

Electronic and dynamical properties of cobalt monogermanide CoGe phases under pressure

Surajit Basak,^{1,*} Aksel Kobińska,² Małgorzata Sternik,¹ Jan Łażewski,¹
Paweł T. Jochym,¹ Andrzej M. Oleś,³ Przemysław Piekarczyk,¹ and Andrzej Ptak^{1,†}

¹*Institute of Nuclear Physics, Polish Academy of Sciences, W. E. Radzikowskiego 152, PL-31342 Kraków, Poland*

²*Department of Physics and Astronomy, Uppsala University, Uppsala SE-75120, Sweden*

³*Institute of Theoretical Physics, Jagiellonian University, Prof. Stanisława Łojasiewicza 11, PL-30348 Kraków, Poland*

(Dated: March 13, 2024)

We present the pressure dependence of the electronic and dynamical properties of six different CoGe phases: orthorhombic Cmmm, hexagonal P6/mmm and P $\bar{6}$ 2m, monoclinic C2/m, cubic P2₁3, and orthorhombic Pnma. Using first-principles DFT calculations and the direct force-constants method, we study the dynamical stability of individual phases under external pressure. We show that the orthorhombic Cmmm and hexagonal P6/mmm structures are unstable over a broad pressure range and most pronounced imaginary phonon soft mode in both cases leads to a stable hexagonal P $\bar{6}$ 2m structure of the lowest ground-state energy of all studied phases at ambient and low (below ~ 3 GPa) external pressure. Under these conditions, the cubic P2₁3 phase has the highest energy, however, together with monoclinic C2/m and orthorhombic Pnma it is dynamically stable and all these three structures can potentially coexist as meta-stable phases. Above ~ 3 GPa, the cubic P2₁3 phase becomes the most energetically favorable. Fitting the Birch–Murnaghan equation of state we derive bulk modulus for all mentioned phases, which indicate relatively high resistance of CoGe to compression. Such conclusions are confirmed by band structure calculations. Additionally, we show that electronic bands of the hexagonal P $\bar{6}$ 2m phase reveal characteristic features of the kagome-like structure, while in the cubic P2₁3 phase spectrum, one can locate spin-1 and double Weyl fermions. In both cases, the external pressure induces the Lifshitz transition, related to the modification of the Fermi surface topology.

I. INTRODUCTION

Exploring the structure of materials is a fundamental first research step in physics, chemistry, and material science. The crystal structure as well as its other properties are inherently determined by bonds between atoms, molecules, or ions. However, a structure exposed to changing external conditions, such as temperature or pressure, may undergo a structural phase transition between different arrangements of atoms, causing the crystal symmetry change. Inspired by the recent discovery of several distinct structures of cobalt monogermanide, we performed an extensive study of stability and pressure dependence of different CoGe crystalline phases.

The CoGe binary compounds are an example of transition metal (TM) monogermanides [1–15]. TM monogermanides are isostructural to TM monosilicides [16–21], but they are more difficult to grow and study [12]. Nevertheless, such compounds have attracted a lot of attention because of the interesting properties observed in different phases. Contrary to MnGe [5, 22, 23] and similarly to FeGe, CoGe does not exhibit magnetic order [5], but can possess intrinsic spin Hall and spin Nernst effects [24]. The surface of CoGe is strongly active and shows bulk oxygen incorporation [25]. Similarly to RhGe [12] or FeGe [8], one can expect that the external conditions can cause a formation of various crystal structures.

Typically, the single crystal of CoGe is grown using a chemical vapor transport method [14]. CoGe can also be synthesized in the cubic FeSi-type structure (B20) at high pressures and temperatures [1, 2]. The cubic phase is a simple, low carrier density, metal, similar to CoSi [5]. Furthermore, the B20 phase was investigated by measuring the specific heat, resistivity, and ⁵⁹Co nuclear magnetic resonance, which uncovered a phase transition at 13.7 K [11]. FeGe also crystallizes with the B20 structure and monoclinic phase. At 893 K, the cubic B20 phase transforms into the CoSn-type structure, which in turn undergoes a transition at 1013 K to the high-temperature monoclinic polymorph, isostructural with CoGe [14]. Furthermore, FeGe exhibits a hexagonal high-temperature P6/mmm structure, while decreasing temperature leads to the cubic P2₁3 structure [8, 26]. High-pressure conditions should favor the cubic B20 structure which has the highest density of all monogermanides polymorphs [2, 14]. Nevertheless, the question of CoGe structure under pressure still remains open. In this work we discuss the crystal stability of CoGe under pressure and its structural, electronic, and dynamical properties.

The paper is organized as follows. Our results are presented and discussed in Sec. II: First, we analyze the investigated crystal structures (Sec. II A). Next, we describe lattice dynamics and system stability at zero pressure (Sec. II B) and under external hydrostatic pressure (Sec. II C). Afterwards, the electronic band structures of the most favorable crystal structures are presented (Sec. III). Finally, we summarize and conclude our findings in Sec. IV. Details of the numerical calculation can

* e-mail: surajit.basak@ifj.edu.pl

† e-mail: aptok@mmj.pl

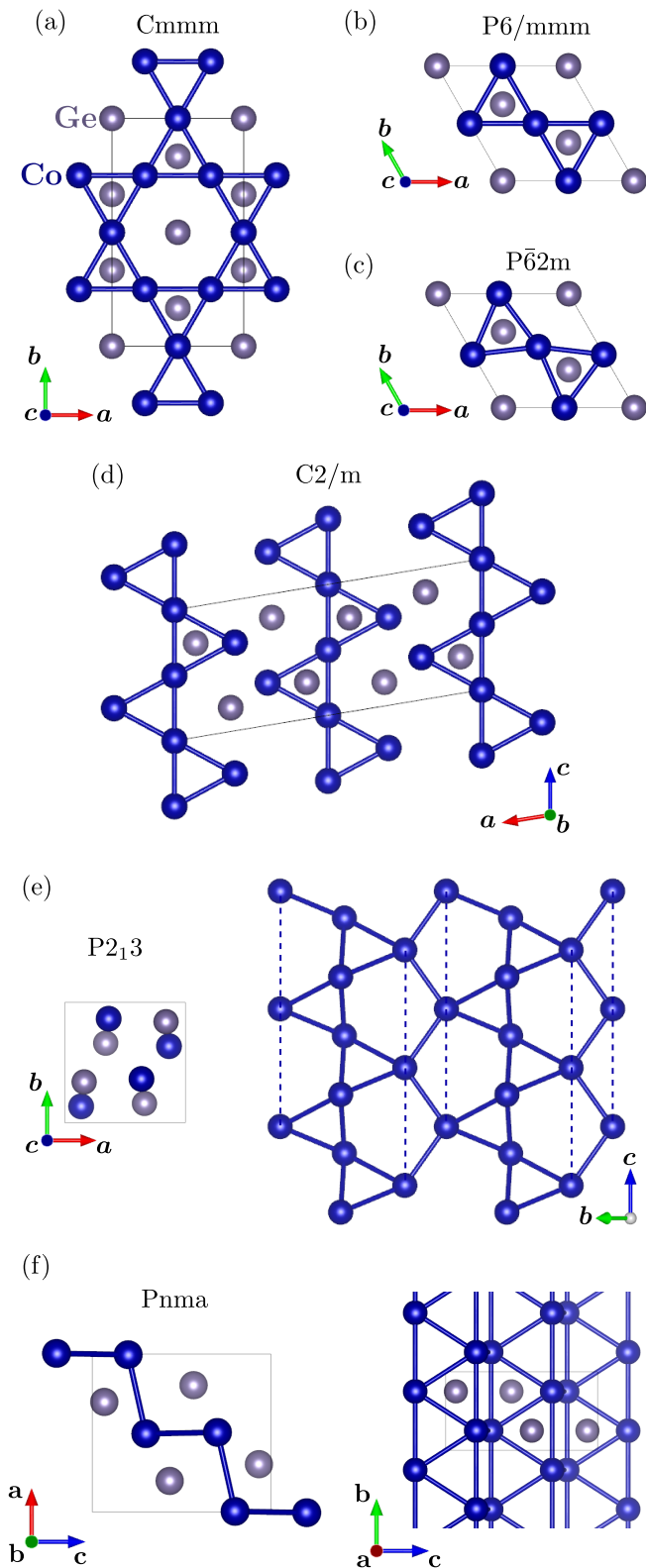


FIG. 1. Overview of CoGe structures: orthorhombic Cmmm (a), hexagonal P6/mmm (b) and P6̄2m (c), monoclinic C2/m (d), cubic P2₁3 (e), and orthorhombic Pnma (f).

be found in App. A

II. SYSTEM STABILITY

A. Crystal structures

As we mentioned in the Introduction, TM monogermanides [1–11] and TM monosilicides [16–21] crystallize within several structures. Early stage study of CoGe suggests existence of monoclinic C2/m [13–15] and cubic P2₁3 (B20) structures [1]. Recently, theoretical studies have also predicted the hexagonal P6̄2m structure [27]. Additionally, one should expect a strong impact of external conditions, such as temperature or pressure, on structure and stability of the material. For example, the crystal structure of FeGe undergoes transformation from the hexagonal P6/mmm to cubic P2₁3 phase with decreasing temperature, around 625 K [8, 26]. Motivated by this, we take up here the topic of stability under pressure of a few plausible structures of CoGe.

Beyond the reported structures (C2/m, P2₁3, and P6̄2m), we also examine following cases:

- Cmmm symmetry, which in OQMD database [28, 29] carries the lowest formation energy [30];
- P6/mmm symmetry – hexagonal (B35) structure, well known from the FeGe system [31], but also reported for CoSn [32] and FeSn [33];
- Pnma symmetry – MnP-like (B31) structure reported for TGe (with T = Ni, Pd, Ir, Pt) [34] and RhGe [35].

The last two symmetries were taken into account due to the chemical affinity of CoGe with other similar systems [36].

All discussed structures of CoGe with different symmetries are presented in Fig. 1. In this group, we can find several similarities. The orthorhombic Cmmm structure [Fig. 1(a)], akin to the hexagonal P6/mmm and P6̄2m symmetries [Fig. 1(b) and 1(c), respectively], contains two-dimensional (2D) kagome(-like) net of Co atoms. The geometry of these structures implies the existence of exotic electronic dispersion relation, containing a flat band, characteristic for a 2D kagome lattice and reported e.g., for CoSn-like compounds [37–45]. The monoclinic C2/m and cubic P2₁3 structures [Figs 1(d) and 1(e), respectively] contain chains of apex-connected Co triangles. A similar structure can also be found in the orthorhombic Pnma symmetry [Fig. 1(f)] with a ladder formed of Co triangles. In those cases, a quasi-one-dimensional (1D) structure should be reflected in the electronic band structure, in form of characteristic for 1D chains electronic bands. Such feature was reported, e.g., in A₂Cr₃As₃ [46–49] or A₂Mo₃As₃ [50–52], where A = K, Rb, and Cs.

After optimization, we found the following lattice parameters:

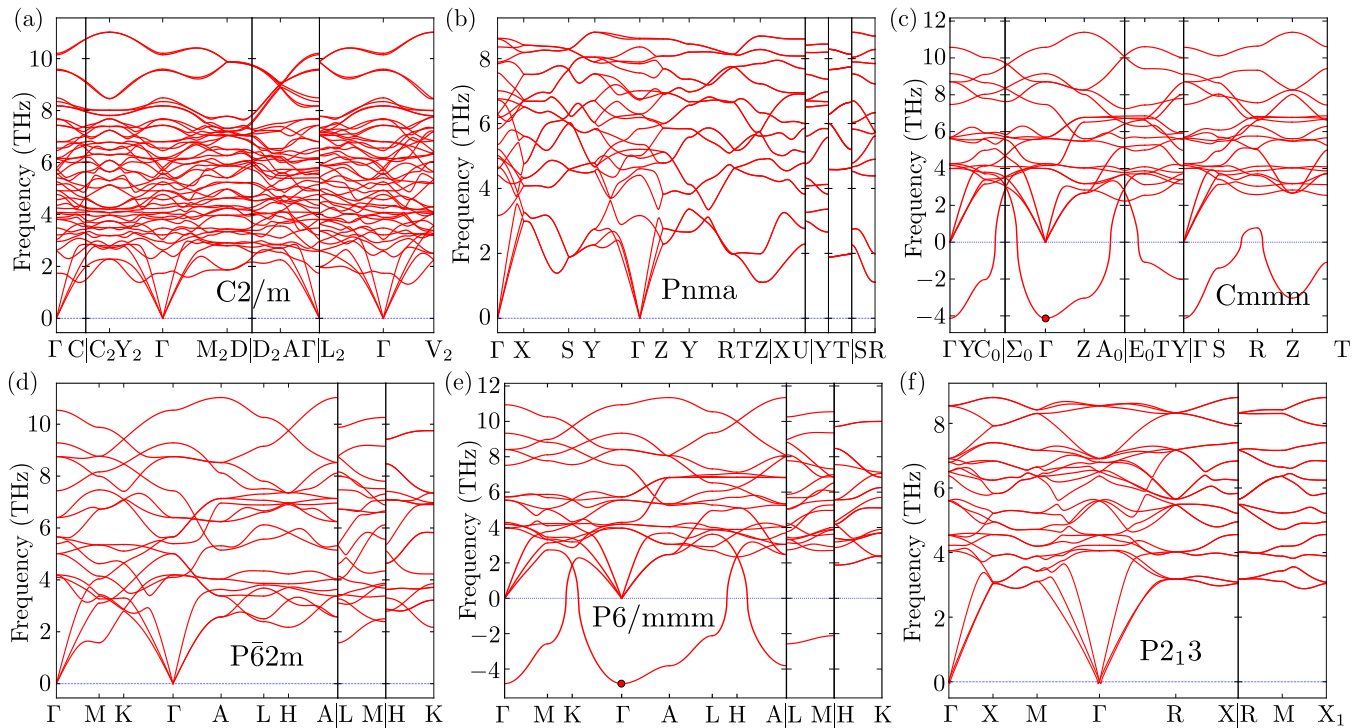


FIG. 2. The phonon dispersion curves of CoGe along the high symmetry directions of considered structures at zero pressure. Corresponding symmetry groups are indicated in the graphs.

The monoclinic C2/m symmetry (space group No. 12): $a = 11.722$ Å, $b = 3.763$ Å, and $c = 4.930$ Å ($\beta = 99.436^\circ$). The Wyckoff positions are: 2a (0,0,0), 4i (0.1964,0,0.3260), and 2c (0,0,1/2) for Co, and 4i (0.8169,0,0.1821) and 4i (0.5693,0,0.2807) for Ge. The lattice constants of the relaxed structures are in good agreement with those reported experimentally for the monoclinic phase [2]: $a = 11.650$ Å, $b = 3.807$ Å, and $c = 4.945$ Å ($\beta = 101.1^\circ$). The lattice parameters are also comparable with the parameters reported for FeGe [14]: $a = 11.838$ Å, $b = 3.937$ Å, and $c = 4.934$ Å ($\beta = 103.514^\circ$).

The orthorhombic Pnma symmetry (space group No. 62): $a = 5.410$ Å, $b = 3.215$ Å, and $c = 6.112$ Å. The Wyckoff positions are 4c (−0.0045,1/4,0.2983) for Co, and 4c (0.8026,1/4,−0.0697) for Ge.

The orthorhombic Cmmm symmetry (space group No. 65): $a = 4.984$ Å, $b = 8.632$ Å, and $c = 3.884$ Å. The Wyckoff positions are 2b (1/2,0,0) and 4e (1/4,1/4,0) for Co, as well as 2a (0,0,0) and 4j (0,2/3,1/2) for Ge.

The hexagonal P62m symmetry (space group No. 189): $a = b = 5.009$ Å, and $c = 3.857$ Å. The Wyckoff positions are 3f (0.4665,0,0) for Co, and 1a (0,0,0) and 2d (1/3,2/3,0) for Ge.

The hexagonal P6/mmm symmetry (space group No. 191): $a = b = 4.987$ Å, and $c = 3.876$ Å. The Wyckoff positions are 3f (1/2,0,0) for Co, and 1a (0,0,0) and 2d (1/3,2/3,0) for Ge.

The cubic P213 symmetry (space group No. 198): $a = b = c = 4.640$ Å. The Wyckoff positions are 4a (0.6360,0.6360,0.6360) for Co, and 4a (0.3394, 0.3394, 0.3394) for Ge. The lattice constant is in a good agreement with the experimental one, ~ 4.635 Å [2, 5, 53] and close to lattice constants of the similar monogermanides: 4.797 Å for MnGe [5] and 4.70 Å for FeGe [14, 54].

B. Zero pressure

To check the system's stability, we calculate the phonon dispersion relations for the symmetries mentioned above (Fig. 2). Since the number of degrees of freedom of the primitive unit cell determines an amount of dispersion relations, the phonon spectrum of C2/m [Fig. 2(a)] is the most complex. Similar crystal structures [containing the kagome-like net, cf. Fig. 1(a)–(c)] exhibit comparable phonon dispersion curves [cf. Fig. 2(c)–(e)]. The phonon frequency ranges for all presented structures are analogous.

Such similarities are also visible in the volume dependence of the ground state energy calculated for systems of different symmetries (Fig. 3). All structures have a comparable volume and nearly the same (within 0.5%) energy per one formula unit. Fitting the Birch–Murnaghan

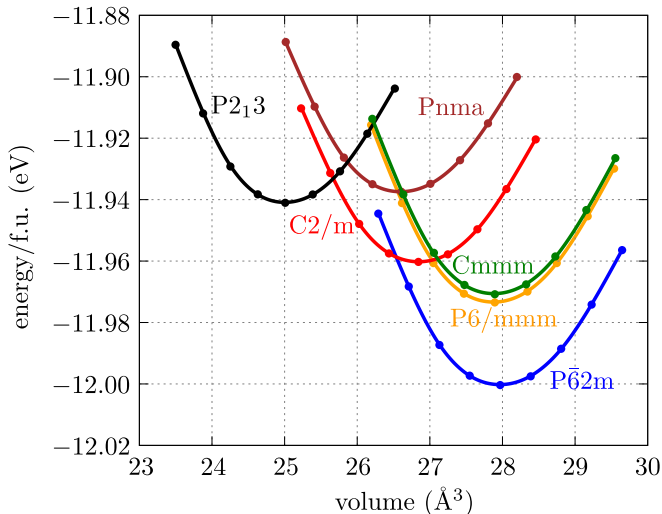


FIG. 3. Volume dependence of the ground-state energy calculated at zero pressure for different structures of CoGe.

equation of state [55]:

$$E(V) = E(V_0) + \frac{B_0 V}{B'_0} \left(\frac{(V_0/V)^{B'_0}}{B'_0 - 1} + 1 \right) - \frac{V_0 B_0}{B'_0 - 1}, \quad (1)$$

to energy versus volume data, we found a bulk modulus B_0 and its pressure derivative B'_0 at the equilibrium volume V_0 (Tab. I). All symmetries are characterized by relatively large bulk modulus, which indicates a weak impact of external pressure on the system's mechanical properties.

Some of the structures discussed above can be eliminated at zero pressure due to instability of harmonic phonons. This applies especially to Cmmm and P6/mmm structures, which show imaginary soft modes at the Γ point. Interestingly, in both structures, this soft mode is associated with the same deformation of the kagome-net, i.e. mutually opposite rotation of the Co triangles forming this sublattice [cf. Figs 1(a) and 1(b) with Fig. 1(c)] around the c axis [27]. After optimization, the distorted kagome lattice in P62m is stable [Fig. 1(c)]

TABLE I. The ground-state energy and equilibrium volume calculated per formula unit, as well as bulk modulus B_0 and its pressure derivative B'_0 fitted with the Birch–Murnaghan equation of state for different structures of CoGe.

Symmetry	B_0 (GPa)	B'_0	energy/f.u. (eV)	volume/f.u. (\AA^3)
C2/m (SG:12)	147.40	3.90	-11.966	26.594
Pnma (SG:62)	142.59	5.76	-11.934	26.346
Cmmm (SG:65)	158.62	4.90	-11.973	27.655
P62m (SG:189)	157.01	4.82	-11.999	27.746
P6/mmm (SG:191)	158.62	4.82	-11.971	27.658
P213 (SG:198)	153.81	6.65	-11.941	24.801

without imaginary frequencies in the phonon spectrum [Fig. 2(d)]. In the final structure, with the $P\bar{6}2m$ symmetry, the Co-triangles within the kagome-like structure are rotated by 4° , which is close to the rotation angle observed experimentally in RhPb [56], i.e. $\sim 4.5^\circ$.

The phonon dispersion curves of the cubic P213 phase [Fig. 2(f)] are similar to those reported for RhGe [12]. Under zero pressure, the cubic P213 (B20) phase has the highest energy among the reported structures (Fig. 3). However, as mentioned earlier, the transition from the hexagonal (P6/mmm) to cubic (P213) symmetry occurs in FeGe also due to temperature increase [8, 26].

C. Role of external pressure

The stability of the system depends on external conditions. Below, we discuss the effect of the external pressure on the system's stability. The comparison of enthalpy (per formula unit) for the discussed symmetries is presented in Fig. 4(a). As the reference level of energy,

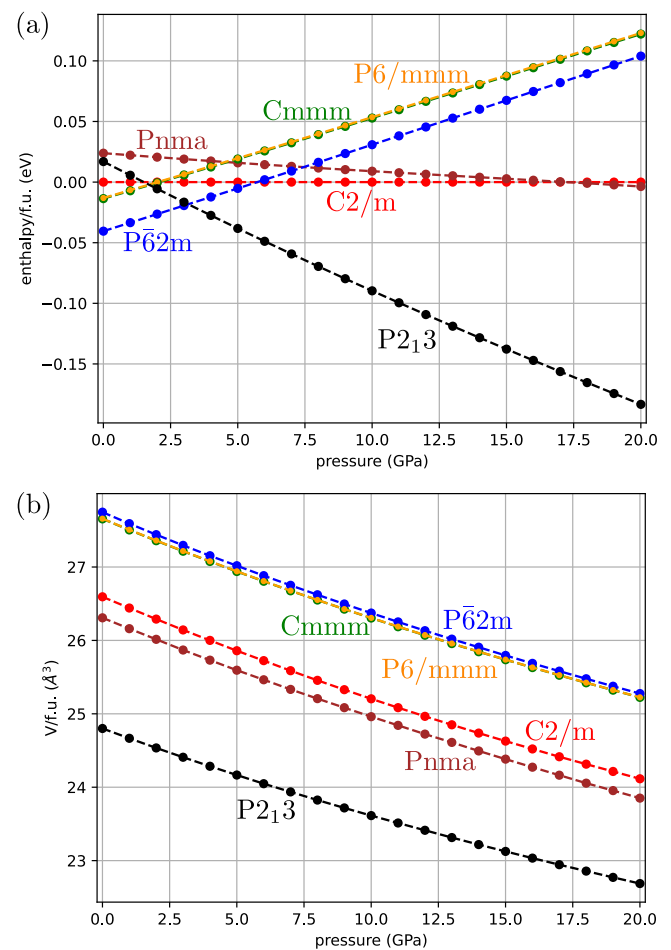


FIG. 4. Pressure dependence of enthalpy (a) and volume (b) calculated (per formula unit) for different CoGe structures (as labeled).

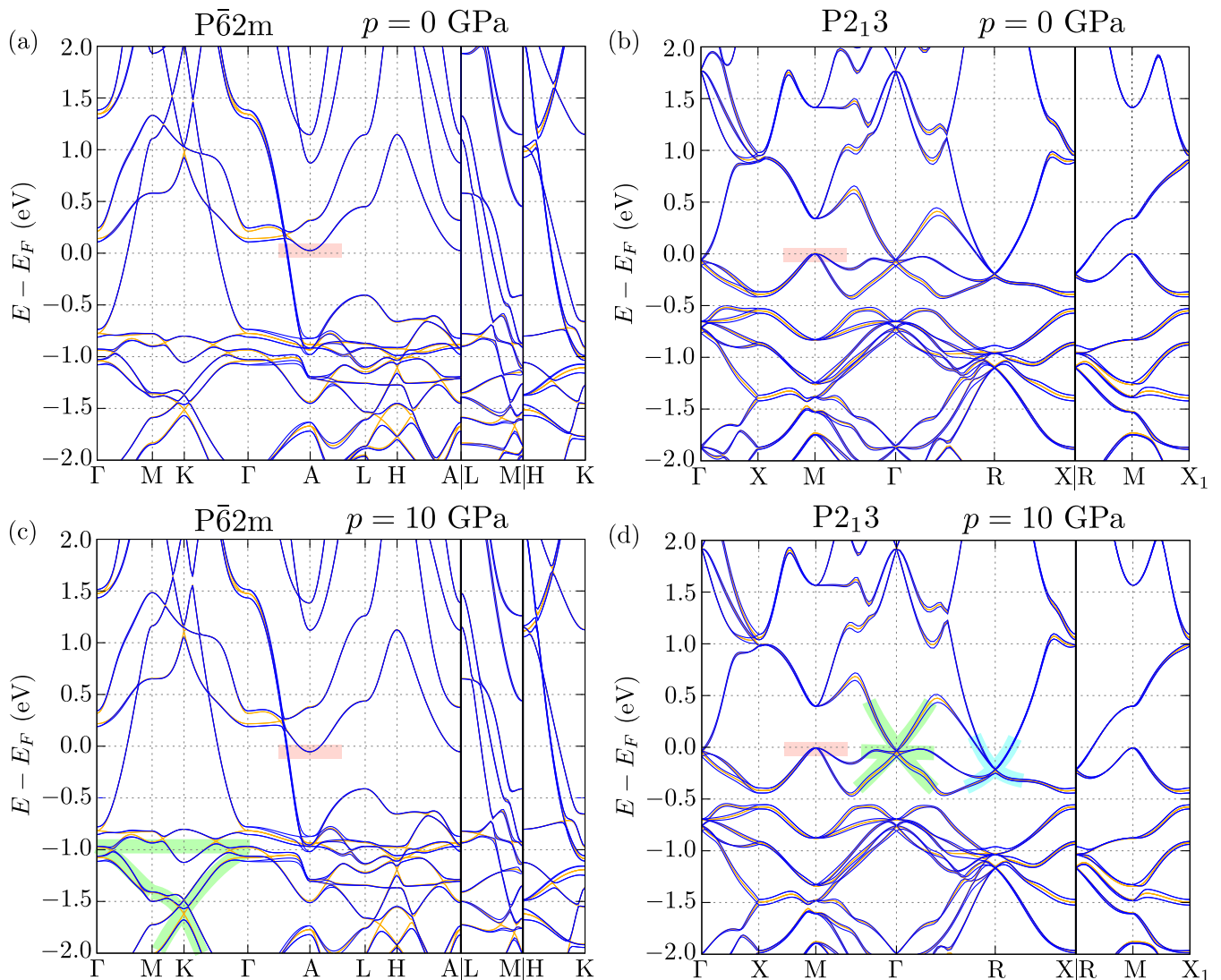


FIG. 5. The top and bottom panels present the electronic band structure in the absence and presence of the external pressure for the hexagonal $P\bar{6}2m$ and cubic $P2_13$ phases (left and right column, respectively). Orange and blue lines correspond to the results obtained with and without spin-orbit coupling, respectively. The $P\bar{6}2m$ band structure contains characteristic kagome-like features [marked by green background color on (c)], while the $P2_13$ exhibits typical spin-1 and double Weyl fermions features [marked by green and blue underground colors on (d), respectively]. Increasing pressure (cf. top and bottom panels) causes the Lifshitz transition [places marked by red background color, at the A point in $P\bar{6}2m$ and the M point in $P2_13$ structure].

we choose the energy of the $C2/m$ structure (red line). At low pressures, the $P\bar{6}2m$ structure is the most favorable energetically. Then, above ~ 3 GPa, the cubic phase has the lowest energy and should be preferred, which is in agreement with the previous predictions [2, 14]. However, regardless of the mutual ground-state energy relations, under specific conditions, crystal can grow in some metastable structures mentioned earlier (i.e. $C2/m$, $Pnma$, or $P2_13$ structure). Based on this, we expect that the experimentally reported monoclinic $C2/m$ phase [14] can come from the cubic $P2_13$ structure at low temperatures.

The unit cell of the unstable $Cmmm$ phase can be constructed by doubling $P6/mmm$ or $P\bar{6}2m$ unit cells. For

the $Cmmm$ and $P6/mmm$ symmetries, the ground-state energies and equilibrium volumes are mostly the same over the entire pressure range (cf. green and orange lines in Figs 3 and 4(a)). However, the imaginary soft mode in the phonon spectra indicates existence of a structure with lower energy. Indeed, our group-theoretical analysis of both soft modes points out at the dynamically stable structure of $P\bar{6}2m$ symmetry with energy systematically lower than those of the $Cmmm$ and $P6/mmm$ phases. Even though all these structures have the same volume under pressure [cf. green, orange, and blue lines on Fig. 4(b)] only the $P\bar{6}2m$ structure is stable over the entire pressure range [cf. blue line with green and orange

lines on Fig. 4(a)].

As expected, due to the relatively large value of bulk modulus, volume (per formula unit) does not strongly depend on pressure [see Fig. 4(b)]. Therefore, independently of the structure symmetry (i.e. arrangement of atoms), the atomic density of systems is approximately the same and inversely proportional to volume. Similarly, all structures exhibit similar compressibility, which is reflected in the relatively weak pressure dependence of volume (independently of the symmetry of the system). For example, the hexagonal $P\bar{6}2m$ structure under external pressure of 10 GPa changes the lattice constants from $a = b = 5.009 \text{ \AA}$ and $c = 3.857 \text{ \AA}$ to $a = b = 4.914 \text{ \AA}$ and $c = 3.790 \text{ \AA}$. Similarly, the cubic $P2_13$ phase lattice constant shrinks from 4.640 \AA to 4.556 \AA . In both cases, the relative modification of the lattice constants induced by such pressure is around $\sim 2 \%$.

Due to small compressibility and volume modification, the orbital overlap does not change much. Consequently, electronic band structures are unaffected by external pressure (see top and bottom panels in Fig. 5). Also, there is only small variation in corresponding phonon dispersion relations (not shown). For example, in the cubic $P2_13$ structure only the frequency of the highest phonon mode at the Γ point is apparently changing from 8.54 THz to 9.29 THz, while the main features of the other phonon dispersion curves remain unchanged.

From the above analysis we can conclude that, under some “critical” pressure (estimated from theoretical calculations as ~ 3 GPa), the studied system transforms from the $P\bar{6}2m$ to $P2_13$ symmetry – similarly to FeGe, which undergoes the phase transition from the hexagonal $P6/mmm$ to cubic $P2_13$ symmetry when temperature decreases [8, 26]. During the described transition, the volume of CoGe increases by about 2.75 \AA^3 per formula unit.

III. ELECTRONIC PROPERTIES

For phases with the lowest energies on the enthalpy vs. pressure graph (Fig. 4), i.e. $P\bar{6}2m$ and $P2_13$, we investigate the electronic band structure. Their dispersion relations (Fig. 5) are characteristic for these symmetries and, generally, a whole class of similar materials. In the case of the hexagonal $P\bar{6}2m$ phase, the electronic band structure exhibits the unique features of a system con-

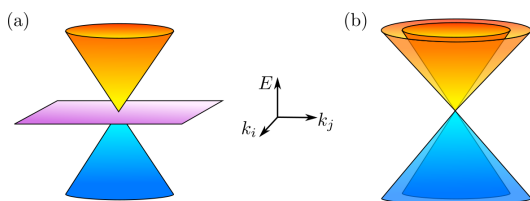


FIG. 6. Schematic band dispersions in 3D E - k space for the spin-1 fermion (a) and double Weyl fermion (b).

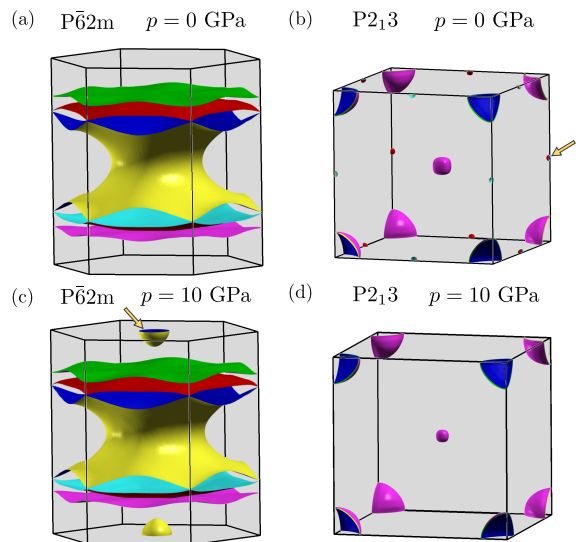


FIG. 7. Modification of the Fermi surface by the external pressure for the hexagonal $P\bar{6}2m$ and cubic $P2_13$ phases (as labeled).

taining “kagome” net. For an ideal kagome lattice, the band structure contains a Dirac crossing at the K point, a strong van Hove singularity at the M point, and an almost flat band [37–45]. We should notice that, contrary to the ideal 2D kagome lattice, where a perfectly flat band is realized, in the three-dimensional (3D) multi-orbital systems the kagome-related “flat” band has a finite bandwidth. The nearly-flat band is mostly associated with the $d_{xz/yz}$ and d_{xy/x^2-y^2} orbitals of Co atoms [38, 39, 42] forming the distorted kagome net [bands marked with the green background line in Fig. 5(c)]. Analogously to CoSn-like compounds, the flat bands are located around -1 eV [38, 45, 56]. In case of the cubic $P2_13$ phase, the electronic band structure exhibits characteristic features of TM monosilicide compounds [19, 20, 57–64], such as features of spin-1 fermions at the Γ point, and double degenerate Weyl points at the R point [marked by green and cyan background lines in Fig. 5(d)]. The spin-1 fermions are related to the crossing of three doubly-degenerate bands (in the absence of spin-orbit coupling). Similarly, one can observe the double Weyl point built by two Dirac-like cones centered at the same point. Both band structures of spin-1 fermions and double Weyl point are presented schematically in Fig. 6. As a consequence, a large Fermi arc is observed in the surface spectral function of CoGe with the cubic structure [53].

The main features of the electronic band structure remain mostly unchanged under pressure. Nevertheless, in both cases, external hydrostatic pressure leads to the Lifshitz transition [65], i.e. change in the Fermi surface topology (see Fig. 7). In both structures, the compression shifts electronic bands and modifies the Fermi surface. In the case of hexagonal $P\bar{6}2m$ structure, new Fermi pockets emerge around the A point [cf. Fig 7(a)

and 7(c)]. On the other hand, in the cubic $P2_13$ structure the small Fermi pocket at the M point disappears under pressure [cf. Fig 7(b) and 7(d)]. Such modifications of the Fermi surface under pressure are related to a relatively small modification of the electronic band structure under pressure. In the hexagonal structure, the bottom of the electron-like band at the A point is shifted to lower energies [cf. the electronic band structure at the A point, marked by a red background in Fig 5(a) and 5(c)]. Similarly, in the case of the cubic structure, the top of the hole-like band at the M point is also shifted to lower energies [cf. the electronic band structure at the M point, marked by the red background in Fig 5(b) and 5(d)].

IV. SUMMARY

In summary, we investigated the stability of several structures of cobalt monogermanide CoGe: monoclinic $C2/m$, orthorhombic $Cmmm$ and $Pnma$, hexagonal $P6/mmm$ and $P\bar{6}2m$, and cubic $P2_13$. From the study of lattice dynamics, we found that the monoclinic $Cmmm$ and hexagonal $P6/mmm$ structures are unstable and have the imaginary soft modes in the phonon spectra. Based on group-theoretical analysis, we reveal that both soft modes lead to the same stable $P\bar{6}2m$ structure, containing the distorted kagome lattice of Co atoms. Surprisingly, under ambient pressure, the $P\bar{6}2m$ structure has the lowest energy among studied phases. The cubic $P2_13$ structure is energetically favored under pressure above ~ 3 GPa.

We also discussed the electronic band structure of the most stable hexagonal $P\bar{6}2m$ and cubic $P2_13$ phases. We demonstrated that the former one shows characteristic features of the compounds containing the kagome net, while the latter exhibits traits of the chiral cubic structure, such as spin-1 fermions and double Weyl fermions. In fact, the $P\bar{6}2m$ structure contains the distorted kagome net of Co atoms, with two triangles forming the kagome-like net rotated in the opposite directions about 4° around the c axis. Furthermore, we show that external pressure weakly affects the main features of the electronic band structure. Nevertheless, the external hydrostatic pressure leads to the Lifshitz transition in both cases.

ACKNOWLEDGMENTS

Some figures in this work were rendered using VESTA [66] and XCRYSDEN [67] software. We kindly acknowledge support by National Science Centre (NCN, Poland) under Project No. 2021/43/B/ST3/02166.

Appendix A: Computational techniques

The first-principles density functional theory (DFT) calculations were performed using the Vienna Ab initio Simulation Package (VASP) code [68–70] with the projector augmented-wave (PAW) potentials [71]. For the exchange-correlation energy, the generalized gradient approximation (GGA) in the Perdew, Burke, and Ernzerhof for solids (PBEsol) parametrization was used [72]. The energy cutoff for the plane-wave expansion was set to 350 eV.

The optimization of the lattice constants and atom positions, including the spin-orbit coupling, was performed in the conventional unit cells. As a convergence condition of the optimization loop, we took the energy change below 10^{-6} eV and 10^{-8} eV for the ionic and electronic degrees of freedom, respectively. The following \mathbf{k} -point grids within the Monkhorst-Pack [73] scheme were used for particular symmetries: $4 \times 12 \times 10$ for monoclinic $C2/m$, $6 \times 5 \times 3$ for orthorhombic $Pnma$, $10 \times 6 \times 12$ for orthorhombic $Cmmm$, $10 \times 10 \times 6$ for hexagonal $P6/mmm$ and $P\bar{6}2m$, and $10 \times 10 \times 10$ for cubic $P2_13$. The symmetries of the system were analyzed using FINDSYM [74] and SPGLIB [75], while momentum space analysis was performed with SEEK-PATH [76].

The dynamical properties were calculated using the direct *Parlinski-Li-Kawazoe* method [77], implemented in PHONOPY package [78, 79]. Within this method, the interatomic force constants (IFC) are calculated from the Hellmann-Feynman (HF) forces generated by displacements of individual atoms inside the supercell. In our calculations, we used the following supercell sizes for different symmetries: $1 \times 3 \times 2$ for monoclinic $C2/m$, $2 \times 1 \times 3$ for orthorhombic $Pnma$, $2 \times 3 \times 2$ for orthorhombic $Cmmm$, $2 \times 2 \times 2$ for hexagonal $P6/mmm$ and $P\bar{6}2m$, and $2 \times 2 \times 2$ for cubic $P2_13$. Phonon calculations were performed with the reduced $4 \times 4 \times 4$ \mathbf{k} -points grid.

-
- [1] V. Larchev and S. Popova, The polymorphism of transition metal monogermanides at high pressures and temperatures, *J. Less-Common Met.* **87**, 53 (1982).
- [2] H. Takizawa, T. Sato, T. Endo, and M. Shimada, High-pressure synthesis and electrical and magnetic properties of MnGe and CoGe with the cubic B20 structure, *J. Solid State Chem.* **73**, 40 (1988).
- [3] H. Wilhelm, M. Baenitz, M. Schmidt, U. K. Rößler, A. A. Leonov, and A. N. Bogdanov, Precursor phenomena at the magnetic ordering of the cubic helimagnet FeGe, *Phys. Rev. Lett.* **107**, 127203 (2011).
- [4] S. V. Grigoriev, N. M. Potapova, S.-A. Siegfried, V. A. Dyadkin, E. V. Moskvina, V. Dmitriev, D. Menzel, C. D. Dewhurst, D. Chernyshov, R. A. Sadykov, L. N. Fomicheva, and A. V. Tsvyashchenko, Chiral properties of structure and magnetism in $Mn_{1-x}Fe_x$ Ge compounds: When the left and the right are fighting, who wins?, *Phys. Rev. Lett.* **110**, 207201 (2013).
- [5] J. F. DiTusa, S. B. Zhang, K. Yamaura, Y. Xiong, J. C. Prestigiacomo, B. W. Fulfer, P. W. Adams, M. I. Brick-

- son, D. A. Browne, C. Capan, Z. Fisk, and J. Y. Chan, Magnetic, thermodynamic, and electrical transport properties of the noncentrosymmetric B20 germanides MnGe and CoGe, *Phys. Rev. B* **90**, 144404 (2014).
- [6] V. A. Sidorov, A. E. Petrova, N. M. Chtchelkatchev, M. V. Magnitskaya, L. N. Fomicheva, D. A. Salamatin, A. V. Nikolaev, I. P. Zibrov, F. Wilhelm, A. Rogalev, and A. V. Tsvyashchenko, Magnetic, electronic, and transport properties of the high-pressure-synthesized chiral magnets $\text{Mn}_{1-x}\text{Rh}_x\text{Ge}$, *Phys. Rev. B* **98**, 125121 (2018).
- [7] F. Zheng, F. N. Rybakov, A. B. Borisov, D. Song, S. Wang, Z.-A. Li, H. Du, N. S. Kiselev, J. Caron, A. Kovács, M. Tian, Y. Zhang, S. Blügel, and R. E. Dunin-Borkowski, Experimental observation of chiral magnetic bobbers in B20-type FeGe, *Nature Nanotech.* **13**, 451 (2018).
- [8] M. J. Stolt, X. Sigelko, N. Mathur, and S. Jin, Chemical pressure stabilization of the cubic B20 structure in skyrmion hosting $\text{Fe}_{1-x}\text{Co}_x\text{Ge}$ alloys, *Chem. Mater.* **30**, 1146 (2018).
- [9] S. Grytsiuk, M. Hoffmann, J.-P. Hanke, P. Mavropoulos, Y. Mokrousov, G. Bihlmayer, and S. Blügel, Ab initio analysis of magnetic properties of the prototype B20 chiral magnet FeGe, *Phys. Rev. B* **100**, 214406 (2019).
- [10] L. V. Kamaeva, N. M. Chtchelkatchev, A. A. Suslov, M. V. Magnitskaya, and A. V. Tsvyashchenko, Structural and thermal stability of B20-type high-pressure phases FeGe and MnGe, *J. Alloys Compd.* **888**, 161565 (2021).
- [11] S.-H. Baek, V. A. Sidorov, A. V. Nikolaev, T. Klimczuk, F. Ronning, and A. V. Tsvyashchenko, Possible quadrupole-order-driven commensurate-incommensurate phase transition in B20 CoGe, *Phys. Rev. B* **105**, 165132 (2022).
- [12] N. M. Chtchelkatchev, M. V. Magnitskaya, and A. V. Tsvyashchenko, Ab initio study of noncentrosymmetric transition-metal monogermanide B20-RhGe synthesized at high temperature and pressure, *Eur. Phys. J. Spec. Top* **229**, 167 (2020).
- [13] S. Bhan and K. Schubert, Zum aufbau der systeme kobalt-germanium, rhodium-silizium sowie einiger verwandter legierungen, *International Journal of Materials Research* **51**, 327 (1960).
- [14] M. W. Richardson, Crystal structure refinements of the B 20 and monoclinic (CoGe-type) polymorphs of FeGe, *Acta Chem. Scand.* **21**, 753 (1967).
- [15] A. Morozkin, Gd-Co-Ge system at 870/1070 K, *Intermetallics* **25**, 136 (2012).
- [16] T. Jeong and W. E. Pickett, Implications of the B20 crystal structure for the magnetoelectronic structure of MnSi, *Phys. Rev. B* **70**, 075114 (2004).
- [17] S. V. Grigoriev, D. Chernyshov, V. A. Dyadkin, V. Dmitriev, S. V. Maleyev, E. V. Moskvina, D. Menzel, J. Schoenes, and H. Eckerlebe, Crystal handedness and spin helix chirality in $\text{Fe}_{1-x}\text{Co}_x\text{Si}$, *Phys. Rev. Lett.* **102**, 037204 (2009).
- [18] S. V. Grigoriev, D. Chernyshov, V. A. Dyadkin, V. Dmitriev, E. V. Moskvina, D. Lamago, T. Wolf, D. Menzel, J. Schoenes, S. V. Maleyev, and H. Eckerlebe, Interplay between crystalline chirality and magnetic structure in $\text{Mn}_{1-x}\text{Fe}_x\text{Si}$, *Phys. Rev. B* **81**, 012408 (2010).
- [19] D. A. Pshenay-Severin, Y. V. Ivanov, A. A. Burkov, and A. T. Burkov, Band structure and unconventional electronic topology of CoSi, *J. Phys.: Condens. Matter* **30**, 135501 (2018).
- [20] Z. Rao, H. Li, T. Zhang, S. Tian, C. Li, B. Fu, C. Tang, L. Wang, Z. Li, W. Fan, J. Li, Y. Huang, Z. Liu, Y. Long, C. Fang, H. Weng, Y. Shi, H. Lei, Y. Sun, T. Qian, and H. Ding, Observation of unconventional chiral fermions with long fermi arcs in CoSi, *Nature* **567**, 496 (2019).
- [21] B. Balasubramanian, P. Manchanda, R. Pahari, Z. Chen, W. Zhang, S. R. Valloppilly, X. Li, A. Sarella, L. Yue, A. Ullah, P. Dev, D. A. Muller, R. Skomski, G. C. Hadjipanayis, and D. J. Sellmyer, Chiral magnetism and high-temperature skyrmions in B20-ordered Co-Si, *Phys. Rev. Lett.* **124**, 057201 (2020).
- [22] O. L. Makarova, A. V. Tsvyashchenko, G. Andre, F. Porcher, L. N. Fomicheva, N. Rey, and I. Mirebeau, Neutron diffraction study of the chiral magnet MnGe, *Phys. Rev. B* **85**, 205205 (2012).
- [23] N. Kanazawa, J.-H. Kim, D. S. Inosov, J. S. White, N. Egetenmeyer, J. L. Gavilano, S. Ishiwata, Y. Onose, T. Arima, B. Keimer, and Y. Tokura, Possible skyrmion-lattice ground state in the B20 chiral-lattice magnet MnGe as seen via small-angle neutron scattering, *Phys. Rev. B* **86**, 134425 (2012).
- [24] T.-Y. Hsieh, B. B. Prasad, and G.-Y. Guo, Helicity-tunable spin hall and spin Nernst effects in unconventional chiral fermion semimetals XY ($X = \text{Co}, \text{Rh}; Y = \text{Si}, \text{Ge}$), *Phys. Rev. B* **106**, 165102 (2022).
- [25] A. J. Pfau, J. Trey Diulus, S. He, G. H. Albuquerque, W. F. Stickle, and G. S. Herman, CoGe surface oxidation studied using X-ray photoelectron spectroscopy, *Appl. Surf. Sci.* **469**, 298 (2019).
- [26] A. Kúkolová, M. Dimitrievska, A. P. Litvinchuk, S. P. Ramanandan, N. Tappy, H. Menon, M. Borg, D. Grundler, and A. Fontcuberta i Morral, Cubic, hexagonal and tetragonal FeGe_x phases ($x = 1, 1.5, 2$): Raman spectroscopy and magnetic properties, *CrystEngComm* **23**, 6506 (2021).
- [27] A. Ptok, A. Kobińska, M. Sternik, J. Łażewski, P. T. Jochym, A. M. Oleś, S. Stankov, and P. Piekarczyk, Chiral phonons in the honeycomb sublattice of layered CoSn-like compounds, *Phys. Rev. B* **104**, 054305 (2021).
- [28] J. E. Saal, S. Kirklin, M. Aykol, B. Meredig, and C. Wolverton, Materials design and discovery with high-throughput density functional theory: The open quantum materials database (OQMD), *JOM* **65**, 1501 (2013).
- [29] S. Kirklin, J. E. Saal, B. Meredig, A. Thompson, J. W. Doak, M. Aykol, S. Rühl, and C. Wolverton, The open quantum materials database (OQMD): assessing the accuracy of DFT formation energies, *npj Comput. Mater.* **1**, 15010 (2015).
- [30] <https://oqmd.org/materials/composition/CoGe>.
- [31] M. W. Richardson, The partial equilibrium diagram of the Fe-Ge system in the range 40-72 at. % Ge, and the crystallisation of some iron germanides by chemical transport reactions, *Acta Chemica Scandinavica* **21**, 2305 (1967).
- [32] A. Larsson, M. Haeberlein, S. Lidin, and U. Schwarz, Single crystal structure refinement and high-pressure properties of CoSn, *J. Alloys Compd.* **240**, 79 (1996).
- [33] J. Waerenborgh, L. Pereira, A. Gonçalves, and H. Noël, Crystal structure, ^{57}Fe Mössbauer spectroscopy and magnetization of $\text{U}_x\text{Fe}_6\text{Sn}_6$ ($0 \leq x \leq 0.6$), *Intermetallics* **13**, 490 (2005).
- [34] H. Pfisterer and K. Schubert, Neue Phasen vom MnP

- (B31)-typ, *Naturwissenschaften* **37**, 112 (1950).
- [35] S. Geller, The rhodium–germanium system. I. the crystal structures of Rh_2Ge , Rh_5Ge_3 and RhGe , *Acta Crystallographica* **8**, 15 (1955).
- [36] H.-C. Wang, S. Botti, and M. A. L. Marques, Predicting stable crystalline compounds using chemical similarity, *npj Comput. Mater.* **7**, 12 (2021).
- [37] B. C. Sales, J. Yan, W. R. Meier, A. D. Christianson, S. Okamoto, and M. A. McGuire, Electronic, magnetic, and thermodynamic properties of the kagome layer compound FeSn , *Phys. Rev. Materials* **3**, 114203 (2019).
- [38] W. R. Meier, M.-H. Du, S. Okamoto, N. Mohanta, A. F. May, M. A. McGuire, C. A. Bridges, G. D. Samolyuk, and B. C. Sales, Flat bands in the CoSn -type compounds, *Phys. Rev. B* **102**, 075148 (2020).
- [39] M. Kang, S. Fang, L. Ye, H. C. Po, J. Denlinger, C. Jozwiak, A. Bostwick, E. Rotenberg, E. Kaxiras, J. G. Checkelsky, and R. Comin, Topological flat bands in frustrated kagome lattice CoSn , *Nat. Commun.* **11**, 4004 (2020).
- [40] M. Kang, L. Ye, S. Fang, J.-S. You, A. Levitan, M. Han, J. I. Facio, C. Jozwiak, A. Bostwick, E. Rotenberg, M. K. Chan, R. D. McDonald, D. Graf, K. Kaznatcheev, E. Vescovo, D. C. Bell, E. Kaxiras, J. van den Brink, M. Richter, M. Prasad Ghimire, J. G. Checkelsky, and R. Comin, Dirac fermions and flat bands in the ideal kagome metal FeSn , *Nat. Mater.* **19**, 163 (2020).
- [41] Z. Lin, C. Wang, P. Wang, S. Yi, L. Li, Q. Zhang, Y. Wang, Z. Wang, H. Huang, Y. Sun, Y. Huang, D. Shen, D. Feng, Z. Sun, J.-H. Cho, C. Zeng, and Z. Zhang, Dirac fermions in antiferromagnetic FeSn kagome lattices with combined space inversion and time-reversal symmetry, *Phys. Rev. B* **102**, 155103 (2020).
- [42] H. Huang, L. Zheng, Z. Lin, X. Guo, S. Wang, S. Zhang, C. Zhang, Z. Sun, Z. Wang, H. Weng, L. Li, T. Wu, X. Chen, and C. Zeng, Flat-band-induced anomalous anisotropic charge transport and orbital magnetism in kagome metal CoSn , *Phys. Rev. Lett.* **128**, 096601 (2022).
- [43] Z. Liu, M. Li, Q. Wang, G. Wang, C. Wen, K. Jiang, X. Lu, S. Yan, Y. Huang, D. Shen, J.-X. Yin, Z. Wang, Z. Yin, H. Lei, and S. Wang, Orbital-selective Dirac fermions and extremely flat bands in frustrated kagome-lattice metal CoSn , *Nat. Commun.* **11**, 4002 (2020).
- [44] M. Han, H. Inoue, S. Fang, C. John, L. Ye, M. K. Chan, D. Graf, T. Suzuki, M. P. Ghimire, W. J. Cho, E. Kaxiras, and J. G. Checkelsky, Evidence of two-dimensional flat band at the surface of antiferromagnetic kagome metal FeSn , *Nat. Commun.* **12**, 5345 (2021).
- [45] B. C. Sales, W. R. Meier, A. F. May, J. Xing, J.-Q. Yan, S. Gao, Y. H. Liu, M. B. Stone, A. D. Christianson, Q. Zhang, and M. A. McGuire, Tuning the flat bands of the kagome metal CoSn with Fe, In, or Ni doping, *Phys. Rev. Materials* **5**, 044202 (2021).
- [46] X. Wu, F. Yang, C. Le, H. Fan, and J. Hu, Triplet p_z -wave pairing in quasi-one-dimensional $\text{A}_2\text{Cr}_3\text{As}_3$ superconductors ($A = \text{K}, \text{Rb}, \text{Cs}$), *Phys. Rev. B* **92**, 104511 (2015).
- [47] X.-X. Wu, C.-C. Le, J. Yuan, H. Fan, and J.-P. Hu, Magnetism in quasi-one-dimensional $\text{A}_2\text{Cr}_3\text{As}_3$ ($A = \text{K}, \text{Rb}$) superconductors, *Chinese Phys. Lett.* **32**, 057401 (2015).
- [48] H. Jiang, G. Cao, and C. Cao, Electronic structure of quasi-one-dimensional superconductor $\text{K}_2\text{Cr}_3\text{As}_3$ from first-principles calculations, *Sci. Rep.* **5**, 16054 (2015).
- [49] C. Xu, N. Wu, G.-X. Zhi, B.-H. Lei, X. Duan, F. Ning, C. Cao, and Q. Chen, Coexistence of nontrivial topological properties and strong ferromagnetic fluctuations in quasi-one-dimensional $\text{A}_2\text{Cr}_3\text{As}_3$, *npj Comput. Mater.* **6**, 30 (2020).
- [50] Y. Yang, S.-Q. Feng, H.-Y. Lu, W.-S. Wang, and Z.-P. Chen, Electronic structures of newly discovered quasi-one-dimensional superconductors $\text{A}_2\text{Mo}_3\text{As}_3$ ($A = \text{K}, \text{Rb}, \text{Cs}$), *J. Supercond. Nov. Magn.* **32**, 2421 (2019).
- [51] K. Zhao, Q.-G. Mu, B.-B. Ruan, M.-H. Zhou, Q.-S. Yang, T. Liu, B.-J. Pan, S. Zhang, G.-F. Chen, and Z.-A. Ren, A new quasi-one-dimensional ternary molybdenum pnictide $\text{Rb}_2\text{Mo}_3\text{As}_3$ with superconducting transition at 10.5 K, *Chinese Phys. Lett.* **37**, 097401 (2020).
- [52] B.-H. Lei and D. J. Singh, Multigap electron-phonon superconductivity in the quasi-one-dimensional pnictide $\text{K}_2\text{Mo}_3\text{As}_3$, *Phys. Rev. B* **103**, 094512 (2021).
- [53] C. K. Barman, C. Mondal, S. Pujari, B. Pathak, and A. Alam, Symmetry protection and giant Fermi arcs from multifold fermions in binary, ternary, and quaternary compounds, *Phys. Rev. B* **102**, 155147 (2020).
- [54] A. Tsvyashchenko, V. Sidorov, A. Petrova, L. Fomicheva, I. Zibrov, and V. Dmitrienko, Superconductivity and magnetism in noncentrosymmetric RhGe , *J. Alloys Compd.* **686**, 431 (2016).
- [55] C. L. Fu and K. M. Ho, First-principles calculation of the equilibrium ground-state properties of transition metals: Applications to Nb and Mo, *Phys. Rev. B* **28**, 5480 (1983).
- [56] A. Ptok, W. R. Meier, A. Kobińska, S. Basak, M. Sternik, J. Łażewski, P. T. Jochym, M. A. McGuire, B. C. Sales, H. Miao, P. Piekarczyk, and A. M. Oleś, Phononic drumhead surface state in the distorted kagome compound RhPb , *Phys. Rev. Res.* **5**, 043231 (2023).
- [57] P. Tang, Q. Zhou, and S.-C. Zhang, Multiple types of topological fermions in transition metal silicides, *Phys. Rev. Lett.* **119**, 206402 (2017).
- [58] G. Chang, S.-Y. Xu, B. J. Wieder, D. S. Sanchez, S.-M. Huang, I. Belopolski, T.-R. Chang, S. Zhang, A. Bansil, H. Lin, and M. Z. Hasan, Unconventional chiral fermions and large topological Fermi arcs in RhSi , *Phys. Rev. Lett.* **119**, 206401 (2017).
- [59] D. S. Sanchez, I. Belopolski, T. A. Cochran, X. Xu, J.-X. Yin, G. Chang, W. Xie, K. Manna, V. Süß, C.-Y. Huang, N. Alidoust, D. Multer, S. S. Zhang, N. Shumiya, X. Wang, G.-Q. Wang, T.-R. Chang, C. Felser, S.-Y. Xu, S. Jia, H. Lin, and M. Z. Hasan, Topological chiral crystals with helicoid-arc quantum states, *Nature* **567**, 500 (2019).
- [60] D. Takane, Z. Wang, S. Souma, K. Nakayama, T. Nakamura, H. Oinuma, Y. Nakata, H. Iwasawa, C. Cacho, T. Kim, K. Horiba, H. Kumigashira, T. Takahashi, Y. Ando, and T. Sato, Observation of chiral fermions with a large topological charge and associated Fermi-arc surface states in CoSi , *Phys. Rev. Lett.* **122**, 076402 (2019).
- [61] N. B. M. Schröter, D. Pei, M. G. Vergniory, Y. Sun, K. Manna, F. de Juan, J. A. Krieger, V. Süß, M. Schmidt, P. Dudin, B. Bradlyn, T. K. Kim, T. Schmitt, C. Cacho, C. Felser, V. N. Strocov, and Y. Chen, Chiral topological semimetal with multifold band crossings and long Fermi arcs, *Nat. Phys.* **15**, 759 (2019).
- [62] H. Li, S. Xu, Z.-C. Rao, L.-Q. Zhou, Z.-J. Wang, S.-M.

- Zhou, S.-J. Tian, S.-Y. Gao, J.-J. Li, Y.-B. Huang, H.-C. Lei, H.-M. Weng, Y.-J. Sun, T.-L. Xia, T. Qian, and H. Ding, Chiral fermion reversal in chiral crystals, *Nat. Commun.* **10**, 5505 (2019).
- [63] M. Yao, K. Manna, Q. Yang, A. Fedorov, V. Voroshnin, B. Valentin Schwarzze, J. Hornung, S. Chattopadhyay, Z. Sun, S. N. Guin, J. Wosnitza, H. Borrmann, C. Shekhar, N. Kumar, J. Fink, Y. Sun, and C. Felser, Observation of giant spin-split Fermi-arc with maximal chern number in the chiral topological semimetal PtGa, *Nat. Commun.* **11**, 2033 (2020).
- [64] A. Bose and A. Narayan, Strain-induced topological charge control in multifold fermion systems, *J. Phys.: Condens. Matter* **33**, 375002 (2021).
- [65] I. M. Lifshitz, Anomalies of electron characteristics of a metal in the high pressure region, *Zh. Eksp. Teor. Fiz.* **38**, 1569 (1960), [*Sov. Phys. JETP* **11**, 1130–1135 (1960)].
- [66] K. Momma and F. Izumi, VESTA3 for three-dimensional visualization of crystal, volumetric and morphology data, *J. Appl. Crystallogr.* **44**, 1272 (2011).
- [67] A. Kokalj, Xcrysden—a new program for displaying crystalline structures and electron densities, *J. Mol. Graph. Model.* **17**, 176 (1999).
- [68] G. Kresse and J. Hafner, Ab initio molecular-dynamics simulation of the liquid-metal–amorphous-semiconductor transition in germanium, *Phys. Rev. B* **49**, 14251 (1994).
- [69] G. Kresse and J. Furthmüller, Efficient iterative schemes for ab initio total-energy calculations using a plane-wave basis set, *Phys. Rev. B* **54**, 11169 (1996).
- [70] G. Kresse and D. Joubert, From ultrasoft pseudopotentials to the projector augmented-wave method, *Phys. Rev. B* **59**, 1758 (1999).
- [71] P. E. Blöchl, Projector augmented-wave method, *Phys. Rev. B* **50**, 17953 (1994).
- [72] J. P. Perdew, A. Ruzsinszky, G. I. Csonka, O. A. Vydrov, G. E. Scuseria, L. A. Constantin, X. Zhou, and K. Burke, Restoring the density-gradient expansion for exchange in solids and surfaces, *Phys. Rev. Lett.* **100**, 136406 (2008).
- [73] H. J. Monkhorst and J. D. Pack, Special points for Brillouin-zone integrations, *Phys. Rev. B* **13**, 5188 (1976).
- [74] H. T. Stokes and D. M. Hatch, FINDSYM: program for identifying the space-group symmetry of a crystal, *J. Appl. Cryst.* **38**, 237 (2005).
- [75] A. Togo and I. Tanaka, SPGLIB: a software library for crystal symmetry search (2018), [arXiv:1808.01590](https://arxiv.org/abs/1808.01590).
- [76] Y. Hinuma, G. Pizzi, Y. Kumagai, F. Oba, and I. Tanaka, Band structure diagram paths based on crystallography, *Comput. Mater. Sci.* **128**, 140 (2017).
- [77] K. Parlinski, Z. Q. Li, and Y. Kawazoe, First-principles determination of the soft mode in cubic ZrO₂, *Phys. Rev. Lett.* **78**, 4063 (1997).
- [78] A. Togo, L. Chaput, T. Tadano, and I. Tanaka, Implementation strategies in phonopy and phono3py, *J. Phys. Condens. Matter* **35**, 353001 (2023).
- [79] A. Togo, First-principles phonon calculations with phonopy and phono3py, *J. Phys. Soc. Jpn.* **92**, 012001 (2023).